Received 13 October 2020; revised 9 November 2020; accepted 11 November 2020. Date of publication 2 December 2020; date of current version 15 January 2021.

Digital Object Identifier 10.1109/OJAP.2020.3041959

3D Printed Wideband Multilayered Dual-Polarized Stacked Patch Antenna With Integrated MMIC Switch

MERVE KACAR [1] (Graduate Student Member, IEEE), THOMAS M. WELLER [2] (Fellow, IEEE), AND GOKHAN MUMCU [1] (Senior Member, IEEE)

[1] Center for Wireless and Microwave Information Systems, University of South Florida, Tampa, FL 33620, USA

[2] School of Electrical Engineering and Computer Science, Oregon State University, Corvallis, OR 97331, USA

CORRESPONDING AUTHOR: M. KACAR (e-mail: mervekacar@usf.edu)

ABSTRACT Capability of 3D printing for developing wideband multilayered antenna systems packaged with active RF circuit components remains relatively unexplored. To address this gap, this manuscript demonstrates wideband patch antenna that is integrated with a polarization selection switch. Antenna bandwidth is enhanced with customized substrate thicknesses and stacked patch layers. Switch is integrated with 3D vertical transitions to achieve wide bandwidth, smaller packaging, and low-loss. To enable future antenna array applications, a detailed investigation is also presented to maximize the performance of the microstrip feed lines by adjusting the substrate thickness and deposition process. The antenna consists of 13 dielectric and conductive layers. Specifically, the manuscript demonstrates the lowest attenuation in the literature for a fully printed microstrip line with 0.25 dB/cm measured loss at 18 GHz. The antenna operates with more than 80% radiation efficiency and 45% bandwidth. The polarization switch is embedded within the antenna structure. The antenna retains a high cross-polarization ratio of $\sim$ 20 dB due to 3D feed line transitions and symmetric location of the switch with respect to the antenna feeds.

INDEX TERMS 3D printing, 3D interconnect, additive manufacturing, dual-polarized antennas, microstrip antennas, wideband.

I. INTRODUCTION

DIRECT digital manufacturing (DDM) is an additive manufacturing (AM, three-dimensional (3D) printing) technique that builds an object layer-by-layer based on 3D geometry model. DDM has been established as a fabrication technique for several end-use products and provides low-cost, lightweight, conformal solutions [1]. Compared to conventional fabrication methods, DDM does not require many fabrication steps and introduces capabilities that are suitable to pursue innovative design solutions [2]. For RF applications, DDM enables multilayered RF electronics with customized material properties, thicknesses, shapes, metallization patterns and structural packaging. The moderate dielectric losses ($\tan\delta \sim 0.0075$) and conductivities ($\sim 10^6$ S/m) of materials employed in the DDM processes have motivated researches to pursue antenna and transmission line designs operating at frequencies ranging from low GHz to mm-wave bands. Recent literature has investigated DDM of antennas and demonstrated that *fully printed* multilayered antennas with high radiation efficiencies are achievable. These demonstrations are at frequencies below X-band. For example, [3] demonstrates the first known additively manufactured multilayer phased antenna array at 2.45 GHz by utilizing fused deposition modeling (FDM) of acrylonitrile butadiene styrene (ABS) filaments and microdispensing of CB028 silver conductive paste (aka DDM process), where microdispensing refers to high precision deposition of liquid materials. By using DDM and similar material combinations, [4] present a 6 GHz half-wave dipole antenna volumetrically embedded into a dielectric structure. In [5], a multilayer low profile 2.6 GHz antenna utilizing FDM of polycarbonate (PC) and microdispensing of silver ink is presented. Reference [6] demonstrates the effect of infill percentage change on permittivity and loss tangent of ABS fabricated with FDM. References [7], [8] investigates low infill dielectrics for antenna substrates. On

This work is licensed under a Creative Commons Attribution-NonCommercial-NoDerivatives 4.0 License. For more information, see https://creativecommons.org/licenses/by-nc-nd/4.0/

the other hand, antenna demonstrations with DDM operating at or above X-band are not reported. In these bands, antenna demonstrations of additive manufacturing are so-far limited to structures that are *partially printed*. This is achieved by using an additional fabrication step (such as copper cladding, spraying, etc.) for metallization over a dielectric part that is realized with the additive manufacturing technique. For instance, [9], [10] present Ku and Ka-band horn antennas using stereolithography (SLA) of plastics and copper cladding. SLA is not suitable for multilayer antennas as material types are limited to liquid polymers and resins. Selective laser sintering (SLS) provides wider material selection including metals. Reference [11] presents multilayer transmission lines and capacitors with SLS; however, each layer requires coating/spraying the surface with dielectric/conductive inks and removing the unsintered material. Reference [12] employs a liquid crystal polymer (LCP) laminate as the host substrate for dielectric and metallic ink layers. While some of the fabrication methods (SLA and metal coating, SLS) are not suitable for multilayer antennas such as microstrip antennas and embedded applications, others (inkjet printing, aerosol jet printing) commonly require a support material as they are not practical for thick substrates.

The major goal in this manuscript is to utilize design flexibilities of DDM for realizing a *fully printed* dual-polarized antenna with radiation efficiency and return loss performances exceeding 80% and 10 dB, respectively, across the Ku-band (12-18 GHz). The antenna should operate with excellent polarization purity and > 25 dB isolation between feed ports. In addition, the antenna must be suitable to be employed as a unit cell within a half-wavelength spaced phased antenna array. Based on the literature review outlined above, meeting these performance metrics implies a significant advancement over the recently reported antennas realized with additive manufacturing. To address the wide bandwidth and dual-polarization needs, an aperture stacked patch antenna fed with microstrip lines is selected for the design. As shown in [13], for antennas operating at lower frequency bands, the antenna substrates are formed from low-infill ratio ABS and their thicknesses are customized to maximize radiation efficiency and bandwidth. However, in contrast to existing literature, this manuscript also investigates the geometry of the microstrip feed lines for the first time to further maximize the radiation efficiency and minimize losses in potential phased array implementations. This is achieved through a detailed investigation of substrate thickness, infill ratio, and infill direction. As such, this manuscript achieves the lowest attenuation (0.25 dB/cm) at 18 GHz with respect to the microstrip lines reported in recent works. Polarization purity is achieved by resorting to the well-known dual-offset feed line excitation through crossed apertures. For improved polarization purity and isolation, the dual-offset microstrip feed lines belonging to the different polarization excitations are located on separate sides of the ground plane. The MMIC switch package (PQFN) is embedded within the structure to make connections with these feed lines using a ramped 3D interconnect approach. Thanks to its shorter line lengths, this interconnect approach is shown for the first time to support a higher return loss (30 dB vs 20 dB) and loss performance over a traditional via based interconnect. The packaging approach also enables the antenna to be utilized within a half-wavelength spaced array. Additional dielectric/conductor layers can be added to the antenna structure to include a MMIC phase shifter package as well, however, the extension to an operational beam-steering phased array is beyond the scope of this article. The fabricated antenna consists of a total of 13 dielectric and conductive layers. As desired, a 45% $S_{11} | < -10$ dB impedance bandwidth is achieved across the entire Ku-band (12-18 GHz) with >80% radiation efficiency. The manuscript is organized as follows: Section II presents the investigation of substrate thickness, infill ratio and infill direction to minimize the loss of the microstrip feed lines utilized in the antenna structure. Section III details the antenna design and 3D printed interconnect performance utilized for MMIC polarization switch inclusion. Experimental verification of the antenna integrated with the MMIC switch is presented in Section IV. Suitability of the antenna element in terms of size and feed line losses for phased array development is demonstrated in Section III. Concluding remarks are provided in Section V.

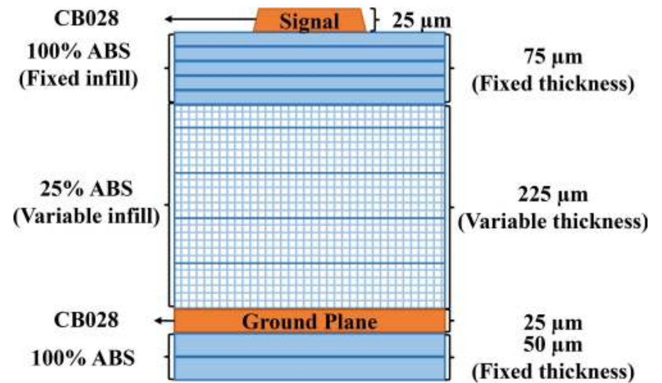

FIGURE 1. Substrate stack-up of the DDM microstrip line.

II. MICROSTRIP LINE CHARACTERIZATION FOR MINIMIZING FEED LINE LOSSES

A. SUBSTRATE STACK-UP

Fig. 1 shows the substrate stack-up of the microstrip lines that are utilized for the antenna feed. ABS, a well-known thermoplastic polymer, is utilized as the dielectric material. The substrate is built up by melting the ABS filament and depositing layer by layer on the printer platform. The goal is to investigate if flexibilities available through the slicing software (i.e., independent control on infill ratio, layer thickness, and printing direction of each layer) can be optimized to minimize the insertion loss (IL) of the microstrip lines. Among these design flexibilities, infill ratio has already been a heavily investigated design parameter for enhancing

antenna performance or achieving control over transmission and reflection properties [14], [15]. Infill ratio refers to the thermoplastic content inside the volume. Naturally, low infill ratio substrates exhibit lower dielectric constants and loss tangents due to the higher air content within the volume. However, as the following section will demonstrate, it is also equally important to consider the line geometry in terms of overall substrate thickness and printing direction to achieve the best possible performance – factors that have not been demonstrated to date to our knowledge. Based on this reasoning, we investigate microstrip lines constructed from ABS with infill ratio down to 25%. In printing studies, we could not go below 25% infill ratio while maintaining good print quality in terms of surface roughness and uniformity. It is also important to note that microdispensing conductive paste over low infill ratio materials is impossible due to paste leakage into the structure. Hence, substrate layers with infill ratios of 100% are necessary under the conductors. In the printing process, it is possible to make trade-offs between the nozzle size of the printing tip and overall printing time. However, thicker layers that can be printed with large nozzle sizes tend to exhibit larger surface roughness. It is already known from other transmission line geometries (such as stripline) that losses due to conductors increase significantly with surface roughness at higher frequencies [16]. Due to these reasons, 100% infill ratio layers that are directly under the microstrip conductor are printed using the minimum available thickness of 15 μm. The total thickness of the 100% infill ratio substrate under the microstrip conductor is taken as 75 μm (i.e., 5×15 μm) since no significant improvement in surface roughness is observed beyond this thickness. In this substrate stack-up, the overall thickness of the 25% infill ratio substrate does not seem to affect the surface roughness of the 100% infill substrate that is directly under the microstrip line conductor. This allows forming the 25% infill ratio substrate in thicker layers to achieve faster printing speed. For the substrate stack-up, the majority of the 25% infill ratio substrate is therefore formed with printing of 50 μm thick ABS layers. The ground plane is microdispensed over a 50 μm thick 100% ABS substrate. Microdispensing of CB028, a silver nanoparticle paste from DuPont, is the technique used in this manuscript to form the conductive traces.

B. DESIGN

Thermoplastic materials have lower loss tangent compared to dielectric inks such as SU-8 ($\varepsilon_r = 2.85$ and $\tan\delta = 0.04$) [17]. However, losses are still higher than standard materials such as hydrocarbon or PTFE ceramic composites, and this increased loss can be challenging for high frequency DDM devices. For high frequency antenna arrays, feed network losses degrade the RF performance, and heating caused by these losses restricts the power handling capabilities. These are the main motivators for investigating the design flexibilities of the DDM process as a whole, not only being based on infill ratio as in references [7], [8], but also based on geometry and printing directions.

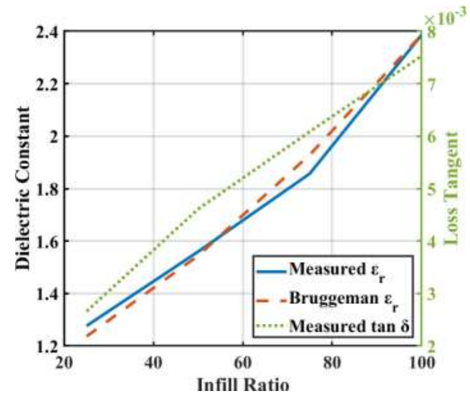

FIGURE 2. Measured dielectric constant and loss tangent for ABS exhibiting different infill ratios. Measurements are averaged across the 4.3 GHz – 17 GHz band.

The dielectric property of the ABS can vary with supplier, color, and frequency [6]. Therefore, before proceeding with microstrip line designs, ABS filament available within our lab has been characterized for dielectric constant and loss tangent values by printing $0.4 \times 3 \times 6$ cm^3 sheets and using a Damaskos 125HC thin sheet tester. Fig. 2. depicts the measurements within the 4.3 GHz – 17 GHz band. Since frequency dependency of dielectric constant and loss tangent is not significant ($<0.1\%$) over this band, Fig. 2 presents the averaged values of the material properties. ABS with 25% infill ratio exhibits a dielectric constant and loss tangent of 1.28 and 0.0027, respectively. As expected, it exhibits the lowest loss tangent justifying the choice of this infill ratio ABS for forming the majority of the microstrip line substrate. On the other hand, ABS with 100% infill ratio exhibits dielectric constant and loss tangent of 2.39 and 0.0075, respectively.

Following the characterization of the ABS material properties, we proceed with the design of the microstrip line geometry. In general, conductor loss decreases with increasing substrate thickness while radiation loss increases. To investigate this, insertion losses of 10 mm long 50 Ω microstrip lines for different substrate thicknesses and infill ratios are simulated using Ansys HFSS. To achieve 50 Ω characteristic impedance for the microstrip line over the substrate stack-up, line width is parametrically swept to achieve a return loss value exceeding 30 dB. In these simulations, conductivity of CB028 silver paste is taken as 1.65 MS/m [13]. Fig. 3 shows the attenuation of these microstrip lines per unit length at 18 GHz – the highest frequency of interest for the antenna designs presented in the following sections. As expected, microstrip lines realized with 25% infill ratio ABS performs the best while at very thin and thick substrates attenuation becomes almost equal with the lines realized over 50% infill ratio substrates due to the dominance of conductive and radiation losses, respectively. Note that microstrip lines are wider on low infill ratio substrates in order to maintain 50 Ω

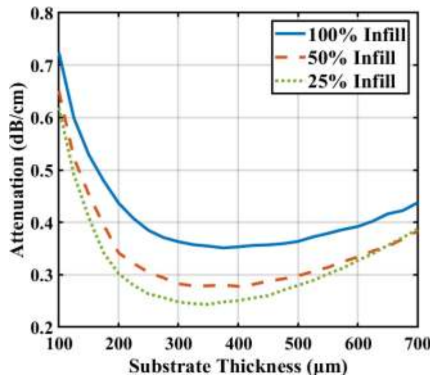

FIGURE 3. Attenuation of microstrip lines for different substrate thicknesses and infill ratios at 18 GHz.

characteristic impedance. Microstrip line loss with the 25% infill ratio substrate remains relatively flat within the range of 300 to 400 μm substrate thicknesses, demonstrating the importance of utilizing the best thickness for minimizing losses. To reduce radiation losses that may occur at line discontinuities, we selected the substrate thickness as 300 μm to implement the microstrip feed lines in the presented antenna realizations. The lowest simulated loss at 18 GHz is 0.25 dB/cm with the 25% infill ratio substrate, a 0.11 dB/cm improvement over the best achievable performance with the optimized 100% infill substrate design. Replacing the CB028 conductivity with copper's conductivity of 58 MS/m in the simulation model shows that the loss at 18 GHz comes down to 0.08 dB/cm from 0.25 dB/cm. Due to this reason, increasing conductivity of 3D printed pastes/inks continues to be an active research area [18], [19].

Another factor that affects the microstrip line attenuation at high frequency is the alignment between the micro dispensed microstrip line and infill direction of the top layer (the direction of the 100% infill ratio ABS filaments deposited to form the top layer that is directly under the signal line as depicted in Fig. 1). The edge roughness of the microstrip line due to this misalignment may introduce additional conductive losses. Reference [20] has demonstrated that surface roughness dependent on the infill direction varies the ohmic losses of microstrip lines at microwave frequencies up to 5 GHz. As frequency increases, it is expected that the current on the microstrip line will be more concentrated in the line edges and therefore the effect of edge roughness will be even more pronounced. Our work in [13], [21] demonstrates this issue through microstrip line characterizations, however, microstrip lines were realized from 100% infill ratio substrates without substrate thickness vs. attenuation considerations. This manuscript demonstrates this effect experimentally with microstrip lines that utilize the 25% infill ratio substrate and optimized substrate thicknesses. Specifically, parallel and perpendicular ABS deposition directions with respect to the microstrip line direction are characterized as shown in Fig. 4. Based on this, the antenna design in Section III utilizes controlled infill

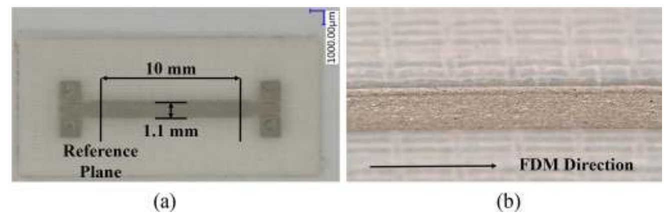

FIGURE 4. Microscope image of (a) the printed microstrip line (b) close-up view of the tilted surface and the microstrip.

directions within its structure to realize the best radiation efficiency performance.

C. FABRICATION

High frequency device fabrication requires further precision as the effect of surface roughness and dimensional variations are more pronounced than at lower frequencies. The surface of substrates fabricated by FDM have waviness due to under-extrusion of the filaments, and this topographical variation degrades the effective RF conductivity of traces deposited on top of them. Reference [22] states that fine-tuning of the extrusion multiplier can achieve smooth surfaces while avoiding over extrusion. 0.97 is found to be the best extrusion multiplier in terms of minimizing surface roughness with the Slic3r slicing software. By incorporating alternating layer thicknesses and fine-tuning the extrusion multiplier, 3 μm peak-to-valley height is achieved within reasonable printing time. All presented devices are printed using an nScrypt 3Dn-Tabletop system including both FDM for dielectric materials and microdispensing for metallization. Dimensional variations due to microdispensing are minimized by decreasing single pass line width and printing speed. For instance, sharper corners are achieved with slower speeds. For a certain line width, air pressure and printing speed are adjusted. Specifically, 100 μm wide single pass lines are microdispensed with 3 psi air pressure at 5 mm/s.

Multilayer structures necessitate good adhesion between silver paste and thermoplastic layers. First, a slurry of ABS and acetone is applied to the surface of the 90°C heated printer bed to improve adhesion to the bed. This eliminates the edge warping of ABS for thick structures. The slurry is also applied on the dried CB028 layers prior to ABS deposition to improve adhesion. CB028 layers are dried at 90°C bed temperature for an hour before ABS deposition. A high nozzle temperature (240°C) for melting the filament is also used for good adhesion.

D. CHARACTERIZATION

Microstrip lines are formed with 10 mm total length with parallel and perpendicular FDM orientation with respect to the line elongation. Fig. 4 shows the microscope images for microstrip lines belonging to parallel FDM orientations. A Keysight N5227A PNA Microwave Network Analyzer is used for taking S-parameter measurements up to 20 GHz. The line excitations are performed with 650 μm

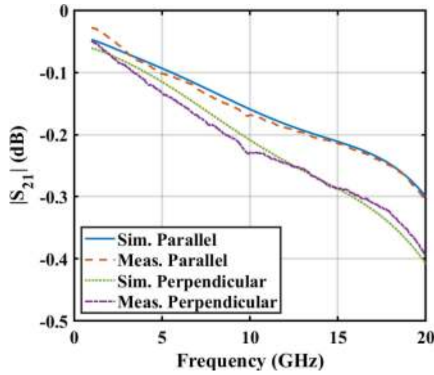

FIGURE 5. Measured and simulated $|S_{21}|$ (dB) of 10 mm long microstrip line with parallel and perpendicular FDM directions.

TABLE 1. Attenuation of transmission lines using additive manufacturing.

Reference	Loss (dB/cm)	Fabrication Technique	Properties
[3]	0.19 at 3 GHz	DDM	Microstrip, ABS, CB028
[23]	2.8 at 20 GHz	Aerosol jet	Stripline, Polyimide, Silver ink
[24]	6 at 20 GHz	Inkjet	Microstrip, SU-8, Silver ink
[25]	0.09 at 5 GHz	SLA, micro-dispensing	Suspended microstrip, SLA resin, CB028
[26]	0.17 at 4 GHz	Polyjet	Microstrip, VeroWhitePlus, Ti/Cu
[13]	0.55 at 18 GHz	DDM	Microstrip, ABS, CB028
This work	0.25 at 18 GHz 0.17 at 10 GHz	DDM	Microstrip, ABS, CB028

pitch ground-signal-ground (GSG) probes. Probe effects are removed from the measurements by utilizing thru-reflect-line (TRL) calibration kits that are designed and printed on the identical substrate stack-up. Fig. 5 depicts the loss performance of the microstrip line samples. It clearly shows that FDM orientation with respect to the line length is an important factor for minimizing the attenuation even though the line geometry in terms of substrate thickness and infill ratio is designed to attain the best performance. Specifically, at the highest end of the Ku-band (i.e., 18 GHz), the loss of the microstrip line increases by 0.08 dB/cm. An RF circuit simulator can be employed to show that such increase in attenuation implies a 60% decrease in the effective RF conductivity. On the other hand, parallel FDM direction with respect to the microstrip line provides the lowest attenuation. Curve fitting as shown in Fig. 5 demonstrates that the measured $|S_{21}|$ performance corresponds to that of a microstrip line exhibiting an effective conductivity of 1.75 MS/m at Ku-band. It is important to note that all characterized microstrip lines exhibit $|S_{11}| < -25$ dB, implying a good impedance match with 50 Ω as they are designed.

Table 1 compares the attenuation of the fully printed microstrip lines reported in this manuscript with data reported in the literature. Microstrip lines fabricated by inkjet and aerosol jet printing of dielectric and silver inks have been characterized in [23], [24] with losses around 2.8-6 dB/cm at 20 GHz. These jet printed microstrip lines demonstrate significantly higher attenuation due to high loss tangent of the dielectric inks utilized in the printing process. References [25], [26] demonstrate loss improvements with suspended microstrip line geometries that employ air substrates. Although [25] demonstrates a slightly lower attenuation than the microstrip lines reported in this work, the suspended line approach requires more than one printing platform and is less practical for implementing multilayered antennas, arrays, and feed networks. Microstrip lines realized over 100% infill ratio ABS have been reported to perform with 0.19 dB/cm and 0.52 dB/cm attenuation at 3 and 18 GHz, respectively [3], [13]. The microstrip line losses reported in this work is 0.07 dB/cm and 0.25 dB/cm at 3 and 18 GHz, respectively. At 18 GHz, this is a 0.27 dB/cm reduction in loss and constitutes the minimum attenuation reported in the literature for microstrip lines that are fully printed using a single manufacturing platform.

III. DUAL-POLARIZED STACKED PATCH ANTENNA

Having established the microstrip line geometry for the antenna feed network, we proceed with the design of the dual-polarized stacked patch antenna to meet the goals indicated in the introduction section, i.e., impedance matching bandwidth across entire Ku-band, compact footprint enabling extension into antenna arrays, dual-polarization and polarization selection capability. Achieving a good cross-polarization level and meeting the compact footprint requirement while employing a cost effective commercial-off-the-shelf SPDT PQFN switch package (MACOM MASW-008322 DC-20 GHz SPDT) necessitates embedding the switch within the antenna structure. Structural embedding of active and control components is generally costly and challenging with multilayered PCB technology. On the other hand, DDM may provide a cost effective approach to realize such embedded RF electronics. The design of the presented antenna with the embedded switch is carried out in two major steps to be able to focus on individual performance aspects: 1) Substrate stack-up and antenna design to maximize antenna performance without considering the switch packaging (Sections III-A and III-B); 2) Switch packaging (Section III-C). Experimental verification is provided in Section IV.

A. SUBSTRATE STACK-UP

Fig. 6(a) shows the substrate stack-up of the antenna. To achieve a low level of cross-polarization, dual offset feed lines are utilized over the crossed coupling apertures. Placement of the feed lines on different sides of the coupling aperture further minimizes the feed line asymmetry within the vicinity of the coupling apertures. Our recent work in [13] already demonstrated an aperture coupled single patch antenna, which can provide 25% impedance matching bandwidth within the Ku-band when implemented with low

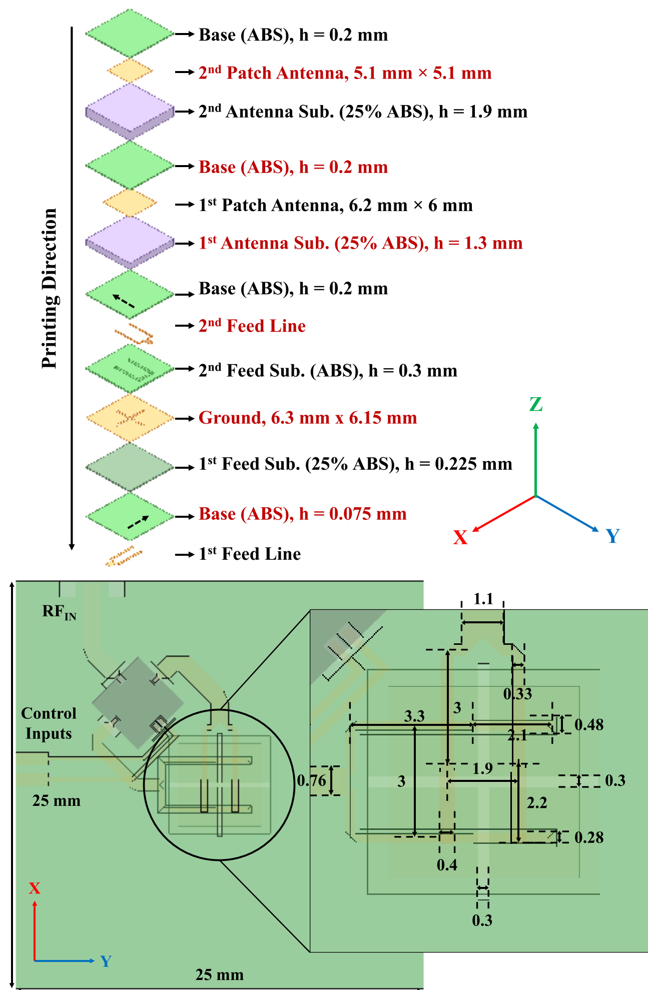

FIGURE 6. (a) Substrate stack-up under the antenna (switch integration is shown in Fig. 10). Dashed arrows show the direction of FDM. (b) 2D view of the feed layout (all dimensions are in millimeters).

infill ratio ABS substrate. An attempt was made to provide dual polarization capability to this earlier antenna by resorting to a square patch geometry. However, inclusion of the crossed coupling apertures and square patch geometry caused a bandwidth reduction that could not be alleviated by adjusting the antenna substrate thickness. Consequently, the antenna was redesigned with the substrate stack-up shown in Fig. 6(a) to exhibit a stacked patch geometry to provide further bandwidth enhancement. The feed substrate thicknesses are selected as 0.3 mm based on the microstrip line loss studies presented in the previous section. Antenna manufacturing is performed from top to bottom starting with the printing of a 200 μm-thick 100% ABS layer and microdispensing of the upper square patch. 25% infill ratio ABS layers with varying thicknesses are utilized as the antenna substrates. The microstrip feed line at the bottom of the stack-up (i.e., 1st feed line in Fig. 6(a)) remains exposed to facilitate the attachment of an edge connector for experiments. 1st feed line is on the same layer of RF signal input to the SPDT switch. Its substrate stack-up is based on Section II-A since

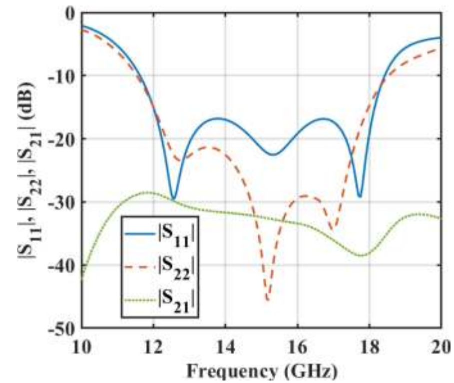

FIGURE 7. Simulated reflection coefficients of polarization 1 and 2 and $|S_{21}|$ (dB).

it may be used to implement long RF feed lines in a full antenna array implementation. The 2nd feed line is embedded within the structure. Due to the layer printing sequence, the substrate of 2nd line is printed after microdispensing of the line conductor. This minimizes the loss by reducing the substrate material under the line. Therefore, a triangular prism-shaped void (200 μm wide and 225 μm deep) is created under the 100 Ω lines. The line widths of 2nd feedline are designed within the full substrate stack-up by performing two-port S-parameter analysis of 10 mm long lines and minimizing the return losses. The antenna has 8 dielectric and 5 conductor layers.

B. ANTENNA DESIGN

First, a single-polarized center-fed aperture coupled square patch antenna is designed to operate at 15 GHz similar to the antenna presented in [13]. The antenna substrate thickness of this design is relatively thick at 2 mm (i.e., $\lambda_0/10$, where λ_0 denotes the free space wavelength at 15 GHz) and it does not meet the impedance bandwidth criteria. Consequently, the substrate stack-up is expanded as shown in Fig. 6 to accommodate a second square patch element. For this stacked aperture-patch geometry and initial dimensions, the design approach reported in [27] is followed to achieve the desired performance goals. Specifically, mutual coupling between the two patches and mutual coupling between the aperture and first patch generate two S_{11} loci in the Smith chart. Adjusting the size of the loci results in 45% $|S_{11}| < -10$ dB bandwidth to cover the Ku-band (12-18 GHz). After the completion of the design for the single-polarized case, the antenna geometry is modified to incorporate dual offset feed lines and a crossed slot aperture to provide dual- polarization capability. Dual-offset feed lines are selected for their low level of cross-polarization performance [28], [29]. To improve the impedance matching performance of the second feed line, the length of the first patch along the second feed line is also slightly increased.

Fig. 7 presents the simulated $|S_{11}|$, $|S_{22}|$, and $|S_{21}|$ performance of the antenna with feed lines extended to the switch. It is observed that, for both polarizations, the antenna operates with more than 45% $|S_{11}| < -10$ dB

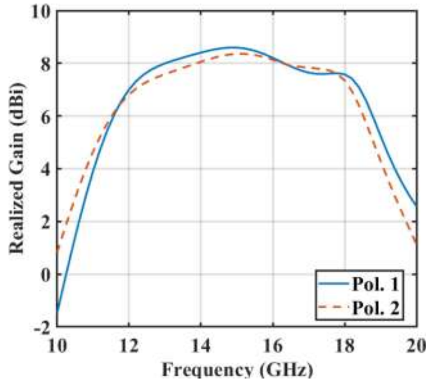

FIGURE 8. Simulated realized gain of the dual-polarized aperture-stacked patch antenna without the switch for both polarizations.

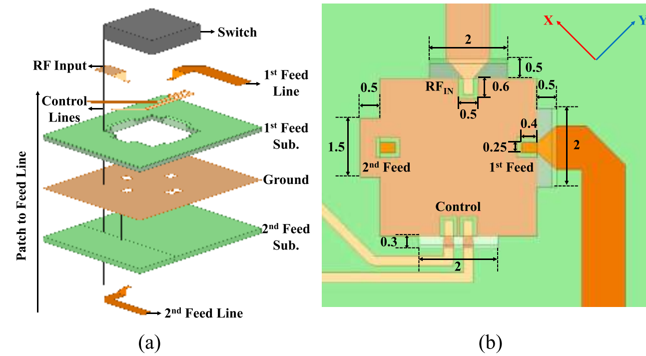

FIGURE 9. (a) Expanded and (b) top view of the switch integration (all dimensions are in millimeters).

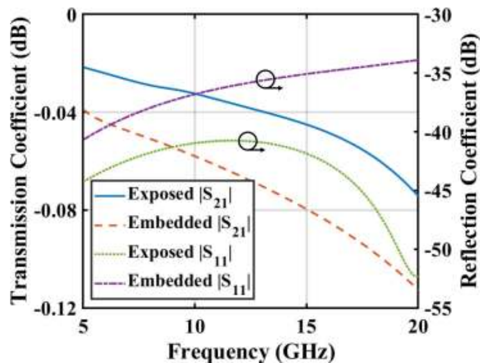

FIGURE 10. Simulated S-parameters of the interconnects.

bandwidth around 15 GHz. The isolation between the polarization feed lines is larger than 28 dB. Fig. 8 presents the simulated broadside-realized gain as a function of frequency for both polarizations. Realized gain attains a peak value of 8.6 dBi and 8.4 dBi at 15 GHz. Realized gain is larger than 6.8 dBi across the impedance matching bandwidth. Simulated radiation efficiency is 87% and 81% at 15 GHz.

C. SWITCH INTEGRATION

A MACOM MASW-008322 DC-20 GHz SPDT switch in PQFN package (4×4 mm^2) is used to select the polarization due to its high isolation performance. According to [30], the

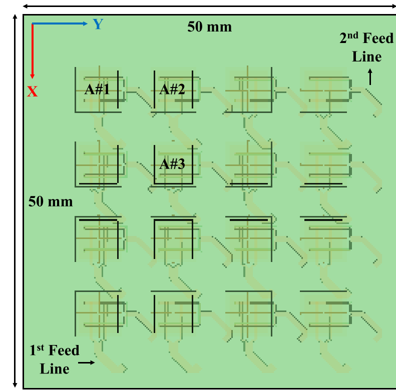

FIGURE 11. Top view of the 4 × 4 antenna array.

switch has more than 40 dB isolation up to 20 GHz, and this is higher than the isolation between antenna feed lines. Fig. 9(a) shows the substrate stack-up around the switch from 3D and 2D perspectives. The PQFN switch package directly lands on the ground plane for minimizing the length of the cross-layer electrical connections for the feed lines. This eliminates the need for vias that would run from the bottom of the PQFN package to the ground plane. The switch package is also placed close to the antenna element to obtain a total footprint of 9×9.5 mm^2. The RF and control pads of the package are isolated from the ground plane by introducing a 0.125 mm gap between the conductive traces. The RF lines are taken to the feed layers #1 and #2 through a ramped transition as illustrated in Fig. 9. The geometry of the ramped transitions is parametrically adjusted to achieve a high return loss. Since feed line #1 and #2 are different (embedded within the stack-up vs. exposed), the transition geometries are slightly different from each other. The transition geometry for the input RF signal line is identical with Feed line #1 since both microstrip lines are on the same layer of the substrate stack-up. As shown in Fig. 10, the return loss is greater than 40 dB for the exposed transition and greater than 33 dB for the embedded microstrip line transitions. Insertion losses of the transitions are less than 0.12 dB.

As stated, the overall footprint size including the SPDT switch makes the antenna element suitable for 2-D array applications. Although a complete phased array manufacturing is beyond the scope of this article, in Fig. 11, we present a potential layout/model for a 4×4 phased array that can harness the designed antenna element. In this model, the antenna elements are excited with lumped ports placed at the switch outputs. In a practical realization, the signal routing for the array can be carried out in a separate layer by transitioning the RF_{IN} signal line from each switch. The design of the RF signal routing should be carried out according to the guidelines (i.e., line width, layer thickness, FDM direction, FDM infill ratio) described in Section II of this manuscript for feed loss minimization. Fig. 12 depicts the simulated impedance matching of antenna elements #1, #2

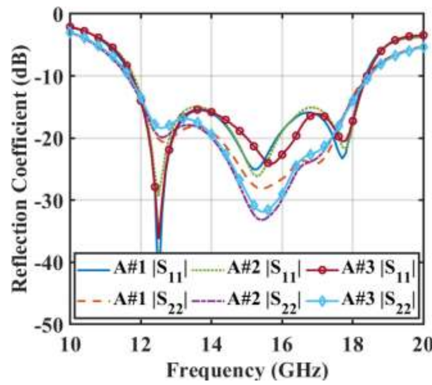

FIGURE 12. Simulated reflection coefficient of the antenna elements #1, #2 and #3.

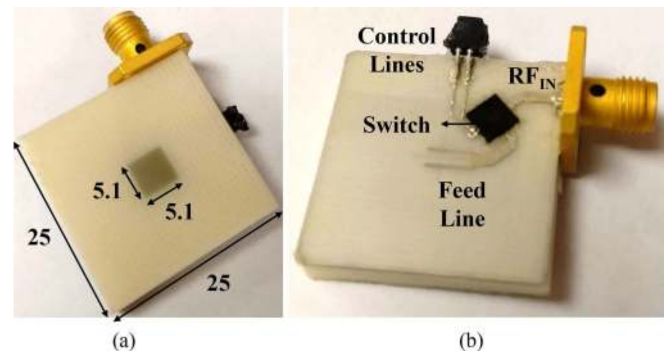

FIGURE 13. (a) Top and (b) bottom view of the fabricated antenna (all dimensions are in millimeters).

and #3. Simulated mutual coupling among the antenna elements is below 12.4 dB, while the highest coupling occurs between 2nd feed line of antenna elements #2 and #3. Simulated broadside realized gain of the array is 16.5 dBi for polarization 1 and 15.6 dBi for polarization 2, implying 83% and 76% radiation efficiency. The half power beam width (HPBW) of the array for polarization 1 is 22.4° in the E-plane and 24.7° in the H-plane. The HPBW of the array for polarization 2 is 22.1° in the E-plane and 24.8° in the H-plane.

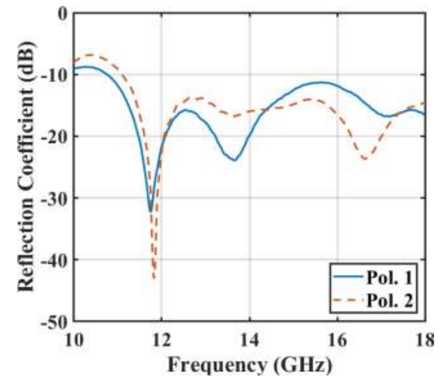

FIGURE 14. Measured reflection coefficient (dB) of the dual-polarized antenna for both polarizations.

IV. EXPERIMENTAL VERIFICATION

Fig. 13 shows the fabricated antenna with SMA connector, socket, and switch. Since the switch is not fully embedded within the structure like in [31], a small droplet of cyanoacrylate glue is used at the corners of the switch package to prevent it from moving. Likewise, the SMA connector and socket packages are mounted to the edge of the substrate using glue instead of screws. Electrical connection from switch pads, SMA connector pin, SMA connector ground, and socket pins to the microdispensed pads/lines are made with H20E (a conductive silver epoxy from EPO-TEK). The assembly is kept in oven at 80°C for 3 hours to cure the H20E. Return loss of the antenna is measured from 10 to 18 GHz using a Keysight E5063A network analyzer. Fig. 14 shows the comparison of measured reflection coefficient of the dual-polarized patch antenna for different switch states. The antenna return loss is greater than 10 dB between 10.8 GHz-18 GHz for polarization 1, and 11.1 GHz-18 GHz for polarization 2; whereas, predicted bandwidth is 45% around 15 GHz. The bandwidth of the antenna element covers the entire Ku-band as expected. There is a good agreement between the simulated and measured results considering that simulated $S_{11}|$ and $S_{22}|$ in Fig. 7 do not include the effect of the switch, connector launch and connector.

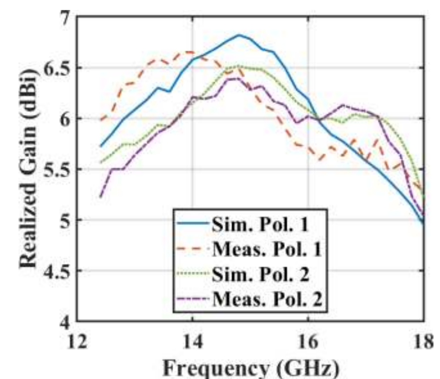

FIGURE 15. Simulated and measured broadside realized gain of the dual-polarized antenna for both polarizations.

Fig. 15 presents the simulated and measured realized gain versus frequency and validates the wideband performance. For realized gain simulations, RF_{IN} and feed line are connected with a mitered bend for each polarization. Switch loss as a function of frequency obtained from manufacturer is subtracted from the simulated realized gain along with 0.4 dB connector loss. When mounted in a 50 Ω transmission line system, the switch exhibits ∼ 1 dB insertion loss at 10 GHz with excellent impedance matching and isolation characteristics (see data sheet [30] for typical frequency dependent characteristics). Simulated realized gain is 6.8 dBi for polarization 1 and 6.4 dBi for polarization 2 at 15 GHz. There is a good agreement between the realized gain results for both polarizations being within 0.7 dB of each other.

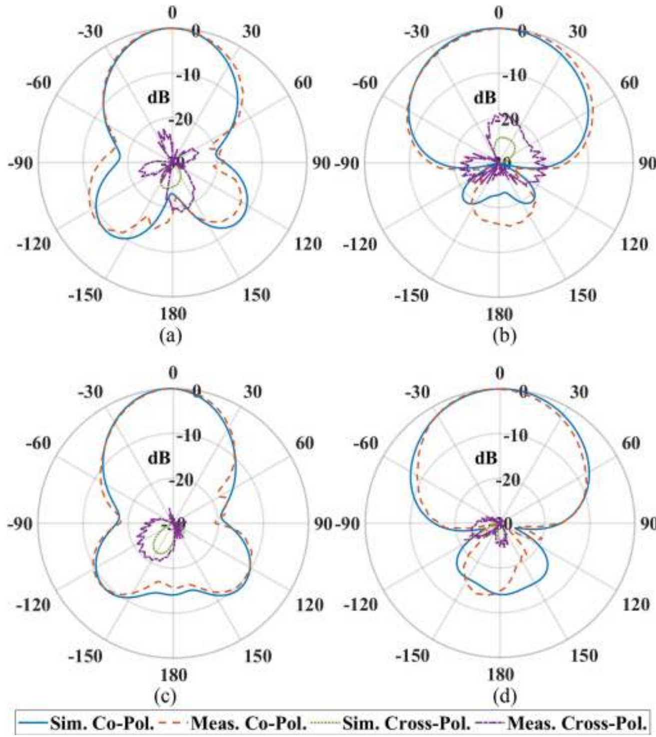

FIGURE 16. Simulated and measured (a) polarization 1 E-plane, (b) polarization 1 H-plane, (c) polarization 2 E-plane and (d) polarization 2 H-plane co-polarization and cross-polarization normalized radiation patterns of antenna at 15 GHz.

Fig. 16 shows the simulated and measured normalized radiation patterns of the antenna element at 15 GHz. Front-to-back radiation ratio for polarization 1 is 18.7 dB for the E-plane and 16.3 dB for the H-plane. For polarization 2, front-to-back ratios of the E-plane and the H-plane are 15.6 dB and 14.9 dB, respectively. Aperture radiation contributes to this front-to-back ratio. However, as demonstrated in reference [31], substrate stack-up can be further expanded by using DDM capabilities to incorporate an embedded cavity for minimizing the back radiation. Cross-polarization gain is lower than the co-polarization gain by 18.7-18.9 dB for the E-plane and 20.2-23.3 dB for the H-plane. Due to the agreement between the simulation and measurement data in radiation patterns and peak realized gains, radiation efficiencies for polarization 1 and 2 can be estimated to be close to the simulated 87% and 81% values.

Table 2 provides a comparison between the antenna presented in this manuscript and additively manufactured antennas available in literature. References [8], [26], [32] demonstrate a hybrid manufacturing approach to realize patch antennas. This approach employs additive manufacturing for antenna substrates, and a damascene process or copper tape for metallization, which require multiple platforms. Reference [7] demonstrates a high radiation efficiency fully inkjet-printed patch antenna utilizing a low infill antenna substrate. However, this work is realized at lower microwave frequencies, where dielectric and conductor losses are not significant. References [30], [31] present 3D-printed patch antennas with high radiation efficiency. However, metallization using ultrasonic wire- embedding requires additional platforms, and thus is not practical for multilayer structures and chip integration. References [3], [5] demonstrate fully-printed dipole antennas on a single platform using DDM. However, these antennas operate at lower microwave frequencies.

TABLE 2. Comparison of antennas using additive manufacturing.

Ref.	Freq. BW	Gain Rad. Eff.	Fab. Techniques	Materials & Antenna Type
[26]	4.49 GHz 4.5%	7.25 dBi NA	Polyjet + Damascene	VeroWhitePlus, Ti/Cu Patch
[32]	6.4 GHz 5%	5.48 dBi NA	SLA + Damascene	Resin, Ti/Cu Patch
[7]	2.4 GHz 8%	8 dBi 81%	Inkjet	UV-Cured Polymer, Silver ink Patch
[8]	2.33 GHz 6%	-3.8 dBi 18%	FDM	NinjaFlex, Copper Tape Patch
[33]	3.58 GHz 7%	4 dBi NA	FDM + wire-mesh embedding	Polycarbonate, Copper, Patch
[34]	7.5 GHz 15%	5.5 dBi/ 84%	FDM + wire- mesh embedding	ABS, Copper, Patch
[5]	2.6 GHz 8%	NA	DDM	PC, Silver ink Dipole over HIS
[3]	2.45 GHz 48%	-2.5 dBi NA	DDM	ABS, CB028 Dipole
This work	15 GHz 45%	6.3 dBi 81-87%	DDM	ABS, CB028, Stacked Patch, **Dual Pol., Packaged IC**

V. CONCLUDING REMARKS

A fully printed multilayer Ku-band aperture-patch antenna is presented. The antenna is fabricated with FDM of ABS and microdispensing of CB028. Custom substrate compositions are utilized to improve the bandwidth, gain and efficiency performance of the antenna. A dual-polarized stacked patch antenna is designed and experimentally characterized to exhibit 6.3 dBi realized gain at 15 GHz, >80% radiation efficiency, and operating with 45% $|S_{11}| < -10$ dB bandwidth. Moreover, the antenna is integrated with a SPDT switch to provide electronic polarization control. Microstrip lines with different geometry and material arrangements are also investigated to minimize line losses. Specifically, fully printed microstrip lines with 0.25 dB/cm measured insertion loss at 18 GHz are demonstrated. The line loss is better than those reported to date in literature. The presented studies shows that the fully printed Ku-band antennas and antenna arrays packaged with control RF electronics (such as switches and phase shifters) is feasible and promising to perform with high radiation efficiency and antenna performance by harnessing the design flexibilities of additive manufacturing.

REFERENCES

[1] R. Sorrentino and O. A. Peverini, "Additive manufacturing: A key enabling technology for next-generation microwave and millimeter-wave systems [point of view]," *Proc. IEEE*, vol. 104, no. 7, pp. 1362–1366, Jul. 2016.

[2] R. Sorrentino, P. Martin-Iglesias, O. A. Peverini, and T. M. Weller, "Additive manufacturing of radio-frequency components [scanning the issue]," *Proc. IEEE*, vol. 105, no. 4, pp. 589–592, Apr. 2017.

[3] T. P. Ketterl *et al.*, "A 2.45 GHz phased array antenna unit cell fabricated using 3-D multi-layer direct digital manufacturing," *IEEE Trans. Microw. Theory Techn.*, vol. 63, no. 12, pp. 4382–4394, Dec. 2015.

[4] D. F. Hawatmeh, S. LeBlanc, P. I. Deffenbaugh, and T. Weller, "Embedded 6-GHz 3-D printed half-wave dipole antenna," *IEEE Antennas Wireless Propag. Lett.*, vol. 16, pp. 145–148, 2017.

[5] P. Pa, Z. Larimore, P. Parsons, and M. Mirotznik, "Multi-material additive manufacturing of embedded low-profile antennas," *Electron. Lett.*, vol. 51, no. 20, pp. 1561–1562, Oct. 2015.

[6] P. I. Deffenbaugh, "3D printed electromagnetic transmission and electronic structures fabricated on a single platform using advanced process integration techniques," Ph.D. dissertation, Dept. Electr. Comput. Eng., Univ. Texas El Paso, El Paso, TX, USA, 2014.

[7] G. McKerricher, D. Titterington, and A. Shamim, "A fully inkjet-printed 3-D honeycomb-inspired patch antenna," *IEEE Antennas Wireless Propag. Lett.*, vol. 15, pp. 544–547, 2016.

[8] S. Moscato *et al.*, "Infill-dependent 3-D-printed material based on ninjaflex filament for antenna applications," *IEEE Antennas Wireless Propag. Lett.*, vol. 15, pp. 1506–1509, 2016.

[9] J. S. Silva, M. García-Vigueras, T. Debogović, J. R. Costa, C. A. Fernandes, and J. R. Mosig, "Stereolithography-based antennas for satellite communications in Ka-Band," *Proc. IEEE*, vol. 105, no. 4, pp. 655–667, Apr. 2017.

[10] M. v. der Vorst and J. Gumpinger, "Applicability of 3D printing techniques for compact Ku-band medium/high-gain antennas," in *Proc. 10th Eur. Conf. Antennas Propag. (EuCAP)*, 2016, pp. 1–4.

[11] H. H. Sigmarsson, E. C. Kinzel, X. Xu, and W. J. Chappell, "Selective laser sintering of multilayer, multimaterial circuit components," in *IEEE MTT-S Int. Microw. Symp. Dig.*, 2006, pp. 1788–1791.

[12] B. K. Tehrani, B. S. Cook, and M. M. Tentzeris, "Inkjet printing of multilayer millimeter-wave Yagi-Uda antennas on flexible substrates," *IEEE Antennas Wireless Propag. Lett.*, vol. 15, pp. 143–146, 2016.

[13] M. Kacar, C. Perkowski, P. Deffenbaugh, J. Booth, G. Mumcu, and T. Weller, "Wideband Ku-band antennas using multi-layer direct digital manufacturing," in *Proc. IEEE Int. Symp. Antennas Propag. USNC/URSI Nat. Radio Sci. Meeting*, 2017, pp. 1243–1244.

[14] M. Ramadan and R. Dahle, "Characterization of 3-D printed flexible heterogeneous substrate designs for wearable antennas," *IEEE Trans. Antennas Propag.*, vol. 67, no. 5, pp. 2896–2903, May 2019.

[15] E. Massoni *et al.*, "3-D printed substrate integrated slab waveguide for single-mode bandwidth enhancement," *IEEE Microw. Wireless Compon. Lett.*, vol. 27, no. 6, pp. 536–538, Jun. 2017.

[16] J. E. Chan, K. Sivaprasad, and K. A. Chamberlin, "High-frequency modeling of frequency-dependent dielectric and conductor losses in transmission lines," *IEEE Trans. Compon. Packag. Manuf. Technol.*, vol. 30, no. 1, pp. 86–91, Mar. 2007.

[17] A. Ghannam, C. Viallon, D. Bourrier, and T. Parra, "Dielectric microwave characterization of the SU-8 thick resin used in an above IC process," in *Proc. Eur. Microw. Conf. (EuMC)*, 2009, pp. 1041–1044.

[18] E. A. Rojas-Nastrucci *et al.*, "Characterization and modeling of K-band coplanar waveguides digitally manufactured using pulsed picosecond laser machining of thick-film conductive paste," *IEEE Trans. Microw. Theory Techn.*, vol. 65, no. 9, pp. 3180–3187, Sep. 2017.

[19] M. Abt *et al.*, "Aerosol-printed highly conductive Ag transmission lines for flexible electronic devices," *IEEE Trans. Compon. Packag. Manuf. Technol.*, vol. 8, no. 10, pp. 1838–1844, Oct. 2018.

[20] J. W. I. Stratton, "A study of direct digital manufactured RF/microwave packaging," M.S. thesis, Dept. Electr. Eng., Univ. South Florida, Tampa, FL, USA, 2015.

[21] M. Kacar, "Direct digital manufacturing of multi-layer wideband Ku-band patch antennas," M.S. thesis, Dept. Electr. Eng., Univ. South Florida, Tampa, FL, USA, 2017.

[22] K. H. Church *et al.*, "Multimaterial and multilayer direct digital manufacturing of 3-D structural microwave electronics," *Proc. IEEE*, vol. 105, no. 4, pp. 688–701, Apr. 2017.

[23] F. Cai, Y. Chang, K. Wang, C. Zhang, B. Wang, and J. Papapolymerou, "Low-loss 3-D multilayer transmission lines and interconnects fabricated by additive manufacturing technologies," *IEEE Trans. Microw. Theory Techn.*, vol. 64, no. 10, pp. 3208–3216, Oct. 2016.

[24] B. K. Tehrani, J. Bito, B. S. Cook, and M. M. Tentzeris, "Fully inkjet-printed multilayer microstrip and T-resonator structures for the RF characterization of printable materials and interconnects," in *Proc. IEEE MTT-S Int. Microw. Symp.*, 2014, pp. 1–4.

[25] P. I. Deffenbaugh, T. M. Weller, and K. H. Church, "Fabrication and microwave characterization of 3-D printed transmission lines," *IEEE Microw. Wireless Compon. Lett.*, vol. 25, no. 12, pp. 823–825, Dec. 2015.

[26] M. I. M. Ghazali, S. Karuppuswami, A. Kaur, and P. Chahal, "3-D Printed air substrates for the design and fabrication of RF components," *IEEE Trans. Compon. Packag. Manuf. Technol.*, vol. 7, no. 6, pp. 982–989, Jun. 2017.

[27] S. D. Targonski, R. B. Waterhouse, and D. M. Pozar, "Design of wide-band aperture-stacked patch microstrip antennas," *IEEE Trans. Antennas Propag.*, vol. 46, no. 9, pp. 1245–1251, Sep. 1998.

[28] C. H. Tsao, Y. M. Hwang, F. Kilburg, and F. Dietrich, "Aperture-coupled patch antennas with wide-bandwidth and dual-polarization capabilities," in *Proc. IEEE AP-S Int. Symp. Antennas Propag.*, vol. 3, 1988, pp. 936–939.

[29] M. Yamazaki, E. T. Rahardjo, and M. Haneishi, "Construction of a slot-coupled planar antenna for dual polarisation," *Electron. Lett.*, vol. 30, no. 22, pp. 1814–1815, Oct. 1994.

[30] "GaAs SPDT switch DC—20 GHz," Data Sheet MASW-008322 [Revision V4], MACOM Technol. Solutions, Lowell, MA, USA. Accessed: Nov. 7, 2020. [Online]. Available: https://cdn.macom.com/datasheets/MASW-008322.pdf

[31] M. Kacar *et al.*, "Phased array antenna element with embedded cavity and MMIC using direct digital manufacturing," in *Proc. IEEE Int. Symp. Antennas Propag. USNC/URSI Nat. Radio Sci. Meeting*, Atlanta, GA, USA, 2019, pp. 81–82.

[32] M. I. M. Ghazali, S. Karuppuswami, S. Mondal, A. Kaur, and P. Chahal, "Embedded actives using additive manufacturing for high-density RF circuits and systems," *IEEE Trans. Compon. Packag. Manuf. Technol.*, vol. 9, no. 8, pp. 1643–1651, Aug. 2019.

[33] X. Yu *et al.*, "3-D printed parts for a multilayer phased array antenna system," *IEEE Antennas Wireless Propag. Lett.*, vol. 17, no. 11, pp. 2150–2154, Nov. 2018.

[34] M. Liang, C. Shemelya, E. MacDonald, R. Wicker, and H. Xin, "3-D printed microwave patch antenna via fused deposition method and ultrasonic wire mesh embedding technique," *IEEE Antennas Wireless Propag. Lett.*, vol. 14, pp. 1346–1349, 2015.

MERVE KACAR (Graduate Student Member, IEEE) received the B.Sc. degree in electrical and electronics engineering from Middle East Technical University, Ankara, Turkey, in 2015, and the M.Sc. and Ph.D. degrees in electrical engineering from the University of South Florida, Tampa, FL, USA, in 2017 and 2020, respectively.

Her research interests include 3D printed antennas, antenna arrays, transmission lines, and advanced packaging techniques.

THOMAS M. WELLER (Fellow, IEEE) received the B.S., M.S., and Ph.D. degrees in electrical engineering from the University of Michigan, Ann Arbor, MI, USA, in 1988, 1991, and 1995, respectively. From 1988 to 1990, he was with Hughes Aircraft Company, El Segundo, CA, USA. From 1995 to 2018, he was a Faculty Member with the University of South Florida, Tampa, FL, USA. In 2018, he joined Oregon State University, Corvallis, OR, USA, where he is currently the Michael and Judith Gaulke Professor and the School Head of electrical engineering and computer science. He co-founded Modelithics, Inc., Tampa, in 2001. His current research interests include tunable and reconfigurable microwave circuits, microwave applications of additive manufacturing and 3-D printing, electromagnetic sensors, passive microwave circuit design, planar and 3-D electrically small antennas, and equivalent circuit modeling.

GOKHAN MUMCU (Senior Member, IEEE) was born in Bursa, Turkey, on March 30, 1982. He received the B.S. degree in electrical engineering from Bilkent University, Ankara, Turkey, in 2003, and the M.S. and Ph.D. degrees in electrical and computer engineering from the Ohio State University, Columbus, in 2005 and 2008, respectively.

He is currently an Associate Professor with the Electrical Engineering Department, University of South Florida, Tampa, FL, USA. From 2009 to 2015, he was an Assistant Professor with the Electrical Engineering Department, University of South Florida. His research interests are additive manufacturing of antennas and phased antenna arrays, reconfigurable antennas and RF devices, microfluidics-based techniques for RF device and antenna reconfiguration, small antennas, and engineered materials.

Dr. Mumcu is the recipient of the 2014 CAREER Award from the U.S. National Science Foundation. He is also recipient of the 2014 Faculty Outstanding Research Award from the University of South Florida, the Best Paper Award at 2008 URSI National Radio Science Meeting, and the 2008 Outstanding Dissertation Award at the Ohio State University, ElectroScience Laboratory. He ranked first on the National University entrance exam taken annually by over 1.5 million Turkish students in 1999. He received the 1999 International Education Fellowship of the Turkish Ministry of Education. He served as the technical program committee chair of the 2013 IEEE International Symposium on Antennas and Propagation, USNC/URSI National Radio Science Meeting, and the 2016 International Workshop on Antenna Technology.